Seismic illumination of small-throw seismogenic faults, Anadarko Basin, Oklahoma

Swetal Patel[1], Folarin Kolawole[1], Jacob I. Walter[2], Xiaowei Chen[1], and Kurt J. Marfurt[1]

Abstract

Substantial increase in the occurrence of injection-induced seismicity across Central and Eastern United States in the past decade, has highlighted a need for novel approaches to geophysical subsurface imaging of potentially seismogenic faults. Active clusters of seismicity illuminate linear fault segments within the sedimentary cover and crystalline basement that were unknown until seismicity began. Such surprises are due to the limited availability of 3D seismic reflection surveys and the difficulty of imaging relatively shallow earthquake events from sparse seismic monitoring arrays. The Sooner Trend Anadarko Basin Canadian Kingfisher Counties (STACK) play of the Anadarko Basin, Oklahoma, provides an opportunity to investigate these earthquake-prone basement faults. Modern high-quality seismic data acquired to map unconventional resource plays in the STACK enable us to assess the detailed subsurface structure. Furthermore, because of increased earthquake risk from anthropogenic activities in the past decade, state regulatory agencies have deployed a dense array of seismic monitoring stations, which allows us to integrate earthquake data with seismic reflection data for analysis of active faulting. We have mapped structural deformation using a suite of seismic attributes, including multispectral coherence, volumetric curvature, and aberrancy, in a 3D seismic reflection data set covering 625 sq mi of the STACK area. To unravel the relationship between the structures and seismicity, we use relocated locally recorded earthquakes and compute the focal mechanism solution for the events. Our results reveal previously unmapped small-throw (<120 m) fault segments with dominant north–south, northwest, and northeast trends, most of which extend from the basement up into the shallower sedimentary Hunton and Woodford Formations. Because of the small offset, we find that aberrancy and the curvature attribute best illuminate the basement-rooted faults in the sedimentary cover. Fault segments with significant vertical offset are better illuminated by band-limited multispectral coherence. We argue that the inherited structure of these faults makes them mostly illuminable by flexure-related seismic attributes, especially within the sedimentary cover. The integration of the illuminated faults with relocated earthquakes and focal mechanism solutions shows that the illuminated faults that have hosted intrasedimentary and/or basement seismicity are reactivated by strike-slip faulting. We hypothesize that careful attribute mapping of faults and related flexures, integrated with recent seismic activity data, and an understanding of the local stress and geomechanical properties, can help mitigate seismic hazards in similar intraplate geological settings where small-throw faults predominate.

Introduction

Within intraplate regions of the earth where low strain rates dominate, an understanding of the presence, distribution, and structure of preexisting faults is important for seismic hazard assessment. The recent spike in intraplate seismicity in the Central and Eastern United States highlights the elevated seismic hazard of the region and has been attributed to unconventional resource exploration and disposal of wastewater into deep sedimentary units that overlie the crystalline basement (Ellsworth, 2013; Weingarten et al., 2015; Machado et al., 2019). Saline water (wastewater) that is co-produced with hydrocarbons is injected into porous and permeable subsurface formations for water flooding to enhance oil recovery and disposal (Walsh and Zoback, 2015). Saltwater injection can cause an increase in the formation pore pressure, promoting fault slip along optimally oriented faults (National Research Council, 2013; Walsh and Zoback, 2015). In addition to wastewater disposal or injection, carbon sequestration (Kaven et al., 2015) and hydraulic fracturing (Holland, 2013a; Skoumal et al., 2015, 2018; Lei et al., 2017; Eyre

[1]University of Oklahoma, School of Geosciences, Norman, Oklahoma 73019, USA. E-mail: swetal.patel@ou.edu (corresponding author); kmarfurt@ou.edu; folarin@ou.edu; xiaowei.chen@ou.edu.

[2]University of Oklahoma, Oklahoma Geological Survey, Norman, Oklahoma 73109-1009, USA. E-mail: jwalter@ou.edu.

Manuscript received by the Editor 25 June 2020; revised manuscript received 21 September 2020; published ahead of production 19 January 2021; published online 27 April 2021. This paper appears in *Interpretation*, Vol. 9, No. 2 (May 2021); p. SE35–SE51, 10 FIGS.
http://dx.doi.org/10.1190/INT-2020-0135.1.

et al., 2019) have also been linked to inducing earthquakes.

Overall, in the Mid-Continent region of the United States, the anthropogenically induced seismicity is most prominent and widespread in Oklahoma, where the susceptibility crystalline basement has been attributed to the preexisting tectonic fabric and frictional stability of the basement fault rocks (Kolawole et al., 2019). The primary wastewater disposal zone is the deep karstified Ordovician Arbuckle Group, which directly overlies the Precambrian granitic basement across most parts of the state. In contrast, the primary hydraulic fracturing targets are the shallower hydrocarbon-rich Devonian–Mississippian sedimentary units. In the past decade, the state of Oklahoma, which initially experienced Mw 3.0 or greater earthquakes events approximately twice a year, recorded 579 and 903 Mw 3.0 or greater earthquakes in 2014 and 2015, respectively (Walter et al., 2020). From 2010 until the present, the Oklahoma Geological Survey (OGS) cataloged more than 34,000 earthquakes (Figure 1a–1c), including 24,840 Mw > 2.0 earthquakes, 2920 Mw > 3.0 earthquakes, and 77 Mw > 4.0 earthquakes (Oklahoma Geological Survey, 1965). Injection-induced seismicity in Oklahoma peaked in 2015, which correlated with the dramatic increase in saltwater injection into the subsurface formation in the same year (Langenbruch et al., 2018). After 2015, market forces and a decrease in the injection rate enforced by the Oklahoma Corporation Commission drove a reduction in the seismic activity rate (Walter et al., 2020). Although the injection-induced seismicity was reduced substantially, Oklahoma experienced the largest-recorded injection-induced seismicity (the 2016 Mw 5.8 Pawnee Oklahoma earthquake; Chen et al., 2017), thus necessitating a need to better understand the structure and stress conditions of preexisting faults.

Currently, the most comprehensive fault database for the state of Oklahoma is the Oklahoma Fault Database (or the "OGS Fault Database," Figure 1a), which has been analyzed for understanding the earthquakes (Marsh and Holland, 2016; Qin et al., 2019). However, this fault database documents a compilation of faults that were mostly mapped in the sedimentary cover by oil and gas companies and those published in the literature (Marsh and Holland, 2016; Qin et al., 2019). It has been found that most of the earthquake epicenters do not occur along these previously mapped faults (e.g., Figure 1d and 1e; Kolawole et al., 2019).

Marsh and Holland (2016) note that though the database cataloged many faults, the database remains incomplete. This limited knowledge of fault distribution, particularly in distinguishing between the faults that are confined to the sedimentary sequences and those that extend into the basement (basement-rooted), inhibits a robust understanding of the seismic hazard of the region. In addition, the difficulty of identifying potentially seismogenic basement-rooted faults within the shallower sedimentary hydraulic-fracture target zones had been associated with (1) the poor illumination of small-offset faults by legacy 2D seismic reflection surveys, (2) incompatible file formats provided by companies contributing fault interpretations to the OGS fault database (Holloway et al., 2015), and (3) incomplete fault mapping in non-hydrocarbon-prone areas of Oklahoma (Marsh and Holland, 2016). However, large-scale structural analysis of the seismicity, the OGS fault database, and additional basement fault mapping has demonstrated the relationships between the intrasedimentary and basement faults and the influence of major basement-rooted faults on the pore pressure distribution and structural deformation in the surrounding areas (Kolawole et al., 2019; Qin et al., 2019; Firkins et al., 2020).

In this paper, we use a recently acquired high-quality 3D seismic reflection data set to investigate potentially seismogenic basement-rooted small-throw (<120 m) faults in part of Oklahoma that has only started experiencing significant earthquake occurrence in 2015 (much later than most of the state). This area is known as the Sooner Trend Anadarko Basin Canadian Kingfisher Counties (STACK) area of Oklahoma, and it constitutes the primary focus of hydrocarbon exploration operations in recent times due to the vertical stacking of the oil-rich sedimentary intervals. We integrate our 3D seismic analysis with well-relocated recent earthquake hypocenters to better understand the relationships between the reactivated fault segments and those that are yet to be reactivated. We demonstrate that the band-limited multispectral coherence, curvature, and aberrancy seismic attributes are most efficient in delineating small-throw faults and the associated flexural deformation that may indicate fault segments that fall below the seismic resolution. We argue that our approach to fault illumination, presented in this study, can potentially aid safe exploration operations in the region and elsewhere by an initial identification (prior to drilling and fluid injection) of the preexisting faults that could be seismogenic, thus minimizing injection-induced or hydraulic fracturing-induced earthquakes.

Seismicity of the STACK area of Oklahoma

The STACK area of Oklahoma, which is the primary focus of unconventional hydrocarbon exploration operations in recent times, extends from the central to southern parts of the state and is bounded to the east by the north–south-trending Nemaha Fault Zone (Figure 1a). Within the STACK, the primary hydraulic fracturing targets are mostly the hydrocarbon-rich Devonian–Mississippian sedimentary units. Although the broader statewide earthquake activity peaked in 2015 in Oklahoma (Langenbruch et al., 2018), relatively fewer earthquakes were recorded in the STACK during that time (Figure 1b). Most of the events in the area occurred between 2015 and 2019 (Figure 1c), coinciding with the timing of increased unconventional exploration in the area targeting the Woodford and Meramec plays (Shemeta et al., 2019). In total, 1438 earthquakes in the STACK and the adjacent

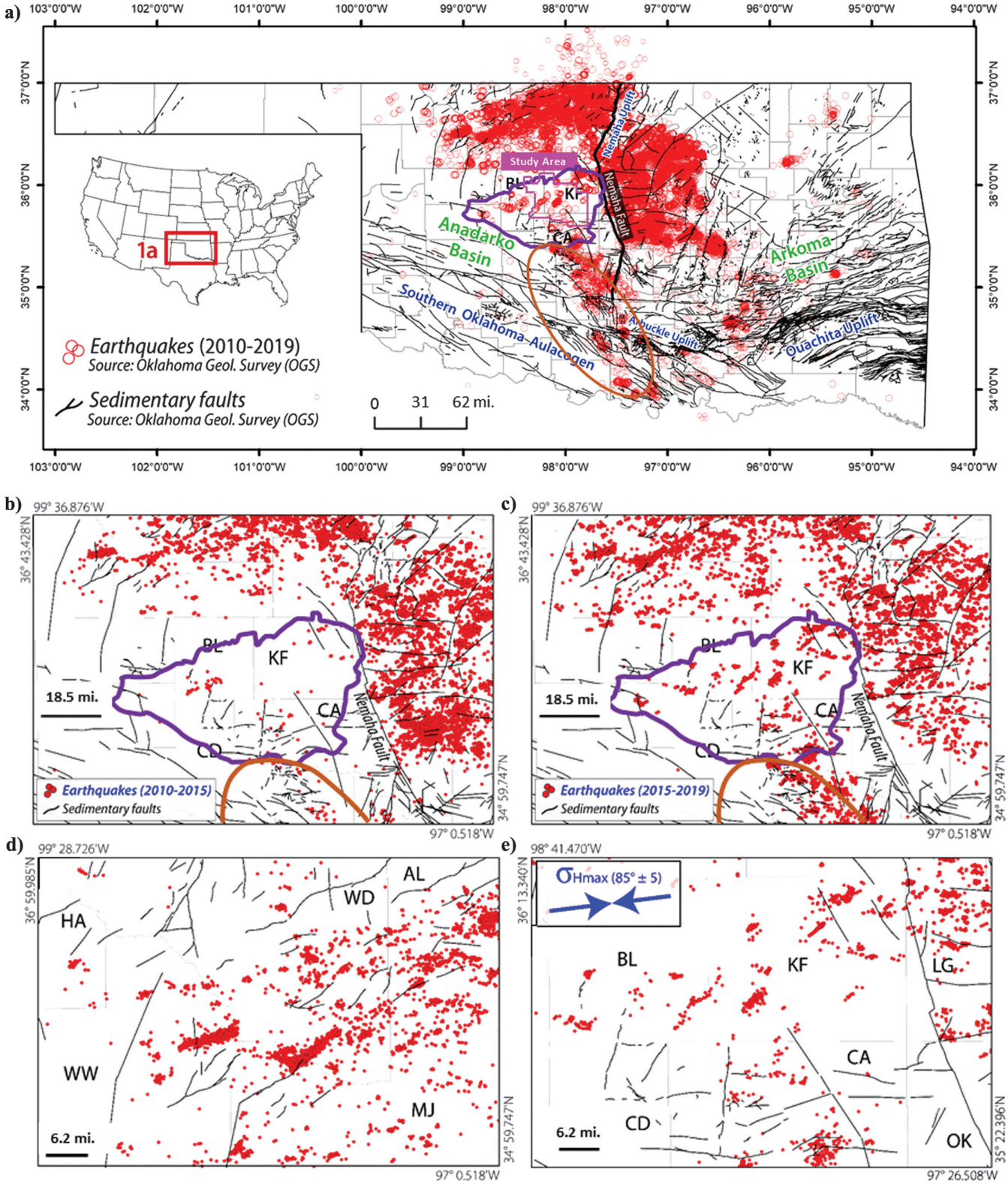

Figure 1. Map of earthquakes that occurred in Oklahoma from 2010 to 2019. The black line shows the faults, the purple and orange lines delimit the STACK and SCOOP plays, respectively, and a thick black line delineates the Nemaha fault. The pink line delineates the 1200 sq mi of the Kingfisher/Loyal 3D survey acquired by TGS in Kingfisher, Canadian, and Blaine Counties. The analysis presented in this paper is a subset of the analysis conducted on the original Kingfisher/Loyal survey. Magnified views of the counties of interest (KF, Kingfisher County; BL, Blaine County; CA, Canadian County; and CD, Caddo County) showing the earthquakes (b) before and (c) after 2015. Note the increase in the number of earthquakes after 2015. (d) A magnified view of (a) from the north of Oklahoma showing that earthquakes in Alfalfa County (AL), Major County (MJ), and Woods County (WD) do not coincide with the currently mapped faults in the region. (e) A similar observation to (d) is observed in the area of interest. ([e] inset) The blue arrows represent the σ_{Hmax} orientation for Kingfisher County (from Qin et al., 2019) (the fault and earthquake data are courtesy of OGS).

South Central Oklahoma Oil Province (SCOOP) (Figure 1a) areas had been associated with recent hydraulic fracturing operations. The largest of these is an Mw 3.6 event in Kingfisher County in mid-2019 (Figure 1c). For this reason, although the bulk of earthquakes in Central Oklahoma may be associated with wastewater disposal, the additional seismic hazard from hydraulic fracturing-induced earthquakes in the STACK has been highlighted.

The Nemaha Fault Zone separates major seismic zones in Central Oklahoma to the west and east sides and represents a statewide pressure boundary (Qin et al., 2019). Also, proximal to the Nemaha Fault Zone, there is increased potential for basement faults to extend up into the sedimentary units and to shallower depths of hydraulic-fracture targets (Firkins et al., 2020). Therefore, there is a need to identify the preexisting faults in the area and better understand the geometric and connectivity relationships between the intrasedimentary and basement fault-related deformation and the influence on seismic hazards of the area.

Geologic setting

The STACK area is located within the Anadarko Basin, Oklahoma. The northeast–southwest-dipping Anadarko Basin is the deepest phanerozoic sedimentary basin in North America (Perry, 1989), composed of Ordovician to Permian sedimentary sequences that unconformably overlie the Precambrian granitic basement (Johnson, 2008). The present depth to the top of the eroded Precambrian basement ranges from 1000 ft in the northeast to 40,000 ft in the southwest (Johnson, 2008). Burke (1977) reports that rifting during the Late Proterozoic extensional tectonics reactivated older Proterozoic and Cambrian faults to create the Mid-Continent Rift and Southern Oklahoma Aulacogen. Perry (1989) provides details on the tectonic evaluation of the Anadarko Basin, dividing the evolution of the Anadarko Basin into four different stages: (1) crustal consolidation and metamorphism during the middle Proterozoic, during which time much of the basement in central Oklahoma was formed by igneous activity, (2) development of the South Oklahoma Aulacogen during the Cambrian Period, (3) development of the southern Oklahoma trough between the Cambrian and the Mississippian, and (4) contractional tectonic deformation of the older sedimentary units and subsidence of the Anadarko Basin as an intracratonic foreland basin during the Late Mississippian to Late Pennsylvanian. The Late Paleozoic contractional deformation peaked in the Late Pennsylvanian time, during which the reactivation of the Precambrian basement faults resulted in folding, faulting, and transpressional deformation of the Phanerozoic sedimentary units (Gay, 2003; McBee, 2003; Kolawole et al., 2020). Hence, the basement faults have been created and reactivated several times during Precambrian, Cambrian, and Late Paleozoic time. The study area, STACK, is bounded by one of these faults, the Nemaha fault (Figure 1a), to the east and west of which faults generally show <120 m vertical offset of stratigraphy (Firkins et al., 2020; Kolawole et al., 2020).

The STACK area has garnered renewed interest due to multiple stacked layers of producible hydrocarbon formations. Figure 2a provides a generalized stratigraphic layout of the Anadarko Basin. The Mississippian Woodford and Meramec are the current target formation for unconventional hydrocarbon exploitation, whereas the Ordovician Arbuckle is the target formation for wastewater injection. The Ordovician to Mississippian formations were deposited on the top of the unconformity created by a brief period of erosion of the earlier Cambrian and Precambrian rocks. This period of erosion was followed by a long geologic time when sediments were deposited as parts of Oklahoma were alternately flooded by shallow seas and then raised above sea level. The Arbuckle Group was deposited during the Late Cambrian to Middle Ordovician time when Oklahoma was submerged entirely; subsequently, thick limestone and dolomite were deposited over the entire state. The Hunton Group was deposited during the Silurian and Early Devonian periods and consisted of limestone and dolomite overlain by black shale. After widespread uplift and erosion forming an erosional unconformity, the Woodford Shale was deposited in the same areas as the Hunton during the Late Devonian and Early Mississippian periods. During the last half of the Mississippian, the basin subsided and led to deposition predominantly of shale with layers of limestone and sandstone. Primary formations deposited during this period are the Caney Shale, the Goddard Formation, and the Springer Formation.

Data and methods

3D seismic reflection data

We analyzed an approximately 1100 sq mi (approximately 2800 sq km) high fold 3D seismic reflection Kingfisher/Loyal survey located in the STACK area of central Oklahoma acquired by TGS (Figure 1a). The analysis shown in the paper uses a subset of the Kingfisher/Loyal survey. The data are devoid of random noise, migration artifacts, and acquisition footprints. The survey is a part of the Gigamerge survey created by combining 20 legacies and seven recent surveys acquired in north-central Oklahoma. Spectral balancing of the seismic volume provided a flat spectrum between 15 and 60 Hz with usable frequencies between 10 and 70 Hz, giving quarter wavelength resolution of 73 ft in the Mississippian formations.

The stratigraphic surfaces (the top of the Mississippian, Meramec, Woodford, and Hunton Formations) were interpreted in the seismic using well tops and seismic well ties (Figure 2b). The depth of the Woodford Formation in the survey ranges from 1470 to 2140 ms. The thickness of the interpreted sedimentary formations decreases toward the northeast and increases toward the southwest. Due to the unavailability of a well-drilled deep enough to the basement, the first continuous reflector above the basement was interpreted as the top of the basement.

To illuminate the structures in the data set, we compute a suite of seismic attributes, including band-limited multispectral coherence, curvature, and aberrancy. Examining horizon slices along the top basement allows us to characterize basement-related structural deformation, whereas horizon slices along the top Hunton provide an assessment of structural deformation in the shallower intrasedimentary sections.

3D seismic attributes

Frequency-dependent multispectral coherence

Seismic coherence is a routine measure to image structural and stratigraphic discontinuities. Chopra and Marfurt (2007) describe several ways to compute waveform dissimilarity in nearby traces. Generally, interpreters prefer to calculate coherence using the broadband amplitude spectrum to image maximum resolvable features. But due to the thickness tuning effect and the variable signal-to-noise ratio (S/N) at different frequencies, coherence computed on specific spectral components can highlight features of certain thicknesses much better than at others (Li et al., 2018). Also, Partyka et al. (1999), Peyton et al. (1998), and Gao (2013) show that different spectral components reveal different geologic details. In the seismic data used in this paper, the 30–55 Hz frequency range revealed smaller as well as larger faults on coherence in the Mississippian formation (Patel and Marfurt, 2019). Adding or subtracting frequencies did not change the resolution of faults in the Mississippian formations. Hence, we computed coherence on the 30–55 Hz spectral components using the approach described by Li et al. (2018). A significant improvement is observed by computing coherence using band-limited data compared to conventional broadband coherence (Figure 3a and 3b).

Volumetric curvature

Although curvature does not map discontinuities, it does map the structural deformation about faults. The curvature will have large positive values for tightly folded anticlines, large negative values for tightly fold synclines, and a zero value for flat or dipping planar features. For 2D structures, the curvature is reciprocal to the radius (r) of the circle that is tangent and best fits

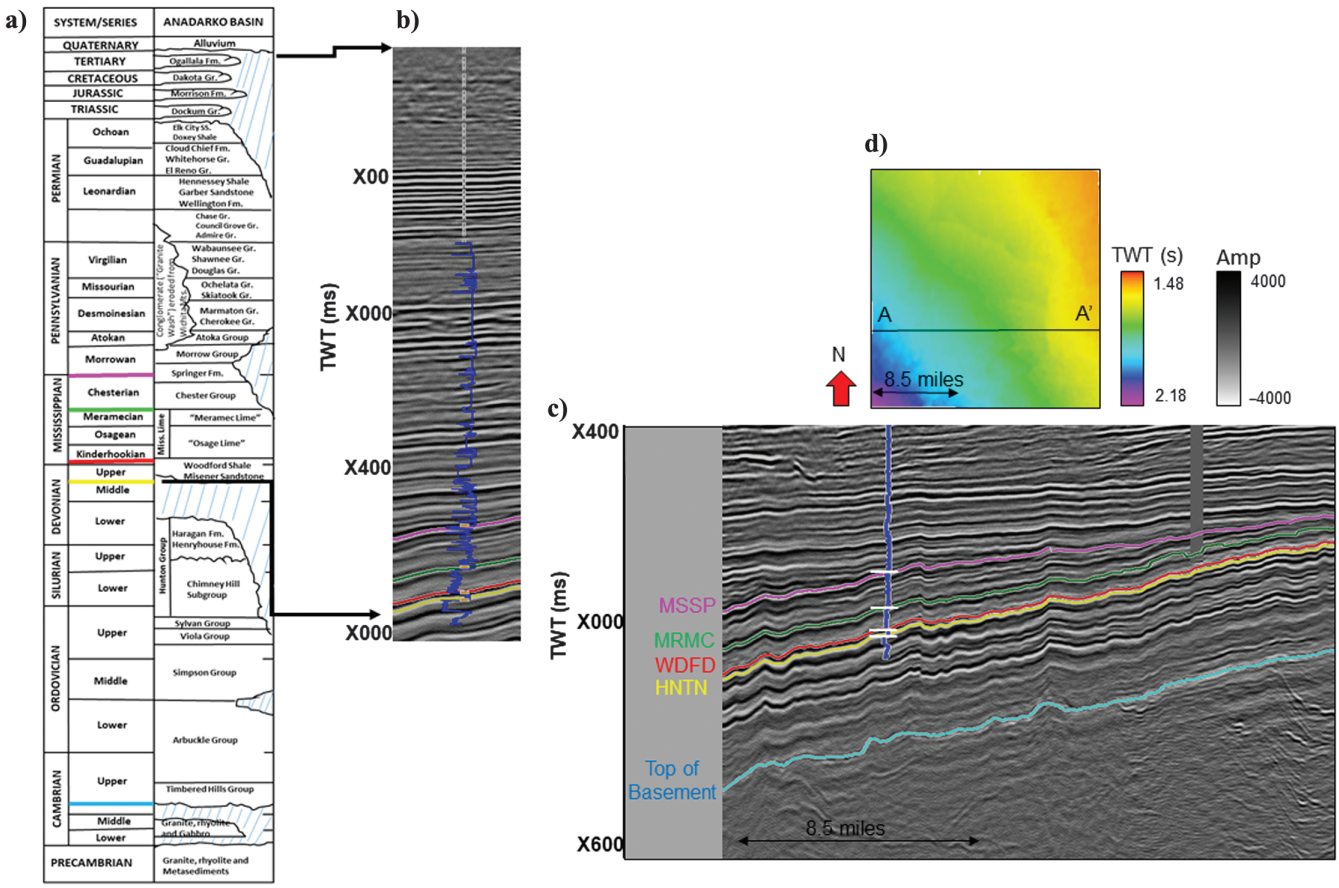

Figure 2. A generalized stratigraphic chart of the Anadarko Basin modified from Johnson and Cardott (1992), showing the formations mapped in the 3D seismic data volume. (b) A magnified view of the seismic cross section near the well. (c) An east–west seismic amplitude cross section in the study area showing the top of the basement and the top of some of the sedimentary sections interpreted using the well tops. The Meramec and Woodford are the most important oil and gas-producing formations in the STACK area for horizontal drilling and artificial fracturing. (d) Two-way traveltime map of the top Hunton from a subset area cropped from the Kingfisher/Loyal survey indicating the location of the cross section shown in (c). (c and d) The STACK area in the Anadarko Basin is a northeast–southwest-dipping basin (the seismic data are courtesy of TGS).

a deformed surface at a particular point (Figure 3d). Figure 3c shows the anticlinal features of the flexures in the basin imaged by k_1 and the synclinal features imaged by k_2. Because the flexures appear conformal over the sedimentary section, unlike coherence, the curvature will image these deformed features across the whole section. The interpretation problem then becomes distinguishing a simple fold from faults whose throw falls below seismic resolution and appears to be a fold. For normal faults, the most-positive k_1 and most-negative curvature k_2 anomalies bracket the fault rather than map the fault surface (Figure 3e). In contrast, aberrancy, the derivative of curvature, better delineates the fault surface.

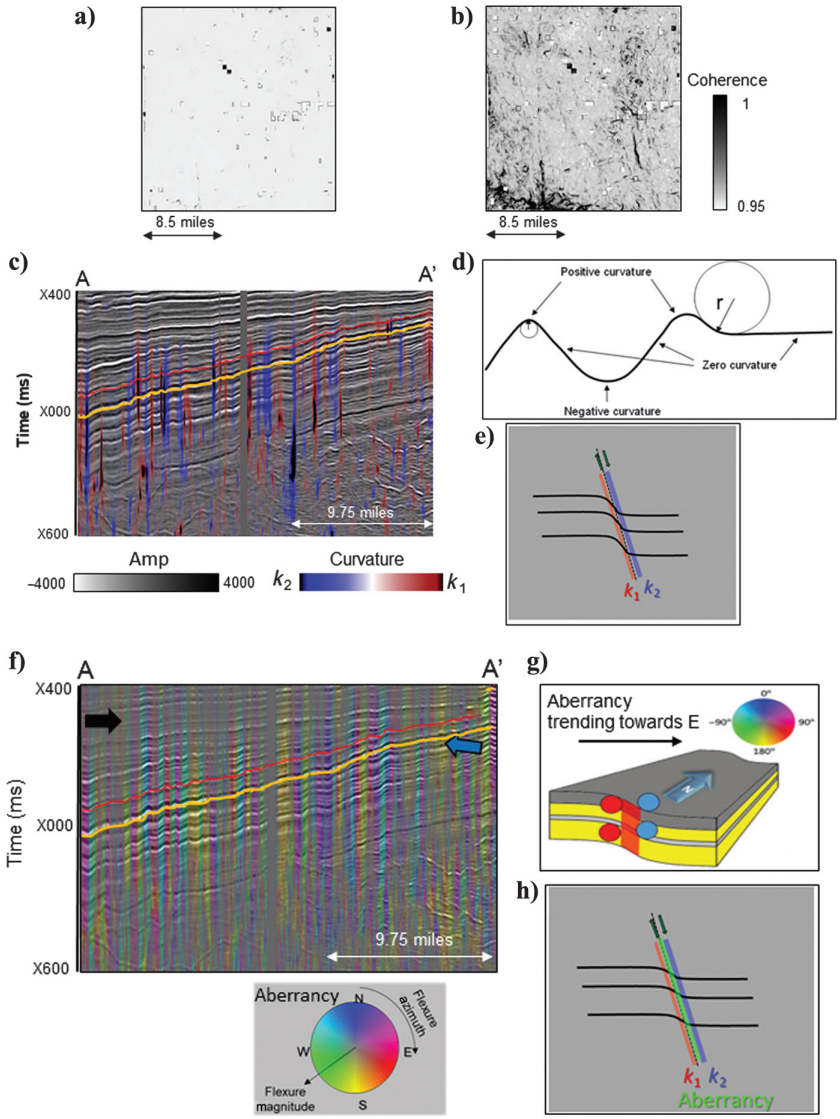

Figure 3. (a) Broadband and (b) band-limited (30–55 Hz) multispectral coherence through Hunton, where (b) provides improved fault images. (c) Seismic amplitude corendered with the most-positive (k_1) and most-negative (k_2) curvature. For normal faults, k_1 delineates the footwall whereas k_2 delineates the hanging wall. The yellow and red lines represent the top Hunton and top Meramec, respectively. (d) A cartoon showing the curvature on a 2D structure. The synclinal feature exhibits negative curvature, generally mapped as a blue anomaly by k_2, whereas the anticlinal feature exhibits positive curvature, mapped as a red anomaly by k_1. Planar features exhibit zero curvature (Chopra and Marfurt, 2007). (e) A cartoon illustrating the concept that k_1 and k_2 will bracket the fault whereas the aberrancy magnitude will image the exact location of the fault. (f) Vertical slice AA′ through the seismic amplitude corendered with the aberrancy vector (defined by a magnitude and azimuth). The planar features appear gray (the black arrow) whereas the strong flexures appear colored, where the color represents the azimuth of the downside of the flexure. The yellow and red lines represent top Hunton and top Meramec, respectively. (g) A cartoon showing that aberrancy measures the lateral change in the curvature (After Qi and Marfurt, 2018). (h) A cartoon showing that for a fault zone whose offset falls below the seismic resolution, the curvature anomalies bracket a fault whereas the aberrancy aligns with the fault trace. For mathematical details on curvature and aberrancy please refer to Appendix A (the seismic data are courtesy of TGS).

Volumetric aberrancy

Aberrancy measures the lateral change in curvature of a picked surface (Qi and Marfurt, 2018). Like curvature, it is also a measure of deformation. In three dimensions, the aberrancy is described by its magnitude and azimuth (Qi and Marfurt, 2018). The magnitude is proportional to the amount of deformation, and the azimuth describes the direction of a decrease in curvature value (Figure 3g). Whereas the dip vector is the first derivative of the structure, the principal curvatures are the second derivative, and the aberrancy is the third derivative of the structure. Automatically computing time-structure maps for every voxel is currently limited only to small zones of interest (Schmidt et al., 2010). However, there are multiple ways to compute volumetric estimates of dip (Chopra and Marfurt, 2007). For this reason, volumetric aberrancy is computed using the second derivatives of the dip vector. Algorithmic details can be found in Gao and Di (2014) and Qi and Marfurt (2018).

In this paper, the azimuth of aberrancy is mapped against the hue axis of an hue, saturation, lightness (HSL) color model represented by a cyclical color bar. The magnitude of the aberrancy is mapped against the saturation axis of the HLS color model. Several interpretation software packages allow mapping any three attributes against HLS. In cases in which this option is not available, a workaround is to corender the aberrancy azimuth and magnitude using opacity, as described by Qi and Marfurt (2018), where the aberrancy magnitude is plotted against the monochrome gray of the gray color. High-magnitude values have low opacity (are transparent), showing the underlying azimuth value, whereas low-magni-

tude values have high opacity and appear gray. Hence, the planar features appear gray whereas the flexures appear colored, corresponding to the aberrancy azimuth values (Figure 3f). Unlike the curvature, the aberrancy magnitude images the fault trace (Figure 3h).

Earthquake data, event relocation, and focal mechanism computation

The OGS has monitored earthquake activity in the state over the past several decades (Walter et al., 2020). The network has expanded in an ad hoc fashion to address monitoring needs as the seismicity rate increased in the past decade. OGS operates over 100 seismometers throughout the state and is the official Advanced National Seismic System regional network within the state, such that USGS catalog events are sourced from OGS. During business hours, analysts manually pick waveform phases and determine compressional wave (P-wave) polarities for regional events within the state, when the S/N allows. Accurate phase picks and P-wave polarities inform precise relocation and focal mechanism determination for events in the study region.

Since July 2010, OGS identified 3438 cataloged earthquakes within the study region defined by the bounds of 35.5° and 36.5° latitude north and 98.5° and 97.5° longitude west. We relocated events using a double-difference algorithm, HypoDD (Waldhauser and Ellsworth, 2000), and we initially chose a velocity model consistent with the one used for OGS routine locations (Walter et al., 2020). We altered the velocity model to be more consistent with known basement and stratigraphic constraints (Crain and Chang, 2018). In addition, we used a V_P/V_S ratio of 1.78 rather than 1.73 to be consistent with available well sonic log information and consistent with a recent relocation study (Schoenball and Ellsworth, 2017). In addition to the relocation, we recomputed focal mechanisms in a uniformly consistent manner using analyst-picked polarities inputted into the HASH program (Hardebeck and Shearer, 2002).

Results

Structures revealed in seismic attribute maps

Figure 5 shows horizon slices along the top basement through a suite of seismic attribute volumes. Figure 6 shows similar horizon slices along the top Hunton. The paleotopographic features are best delineated on band-limited multispectral coherence along the top basement, but the correlation of the attribute with the earthquakes reveals that most earthquakes do not correlate to any mapped coherence anomalies (Figure 5a). The horizon slices through curvatures (Figure 5b) and aberrancy (Figure 5c) provide images of flexures rather than discontinuities. For normal faults with sufficient offset, the coherence anomaly maps the fault trace whereas the most-positive and most-negative curvature anomalies bracket the fault trace. As seismic resolution (or fault offset) decreases, the coherence anomaly disappears, but the curvature anomalies remain. Aberrancy maps the crossing point (flexure) from positive to negative curvature, thereby mapping a hypothesized fault trace. A total of 36, 70, and 76 lineaments were mapped on coherence, curvature, and aberrancy, respectively (Figure 5e). The lineament density is much lower in coherence compared to curvature and aberrancy.

Unlike along the top basement, horizon slices through multispectral coherence along the top Hunton show considerable faulting. However, we do not observe the thickening of the stratigraphic packages towards the faults in the downthrown sides of the faults. The most prominent is the north–south lineament (the purple arrow, Figure 6), imaged by curvature and aberrancy in the top basement. The signature of the paleotopographic features disappears on coherence through the top Hunton. The curvature reveals several new features and improves the continuity of the north–south lineament. Aberrancy im-

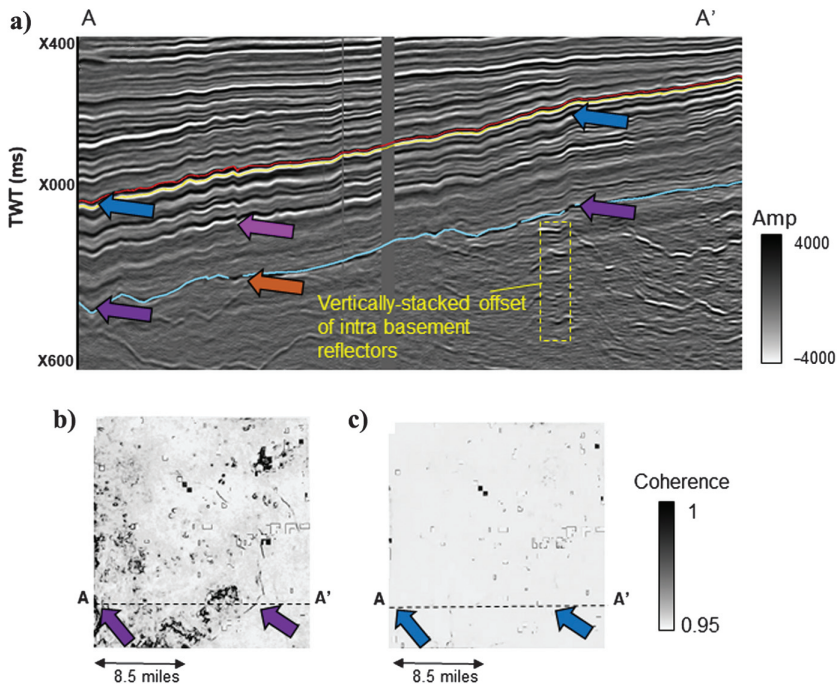

Figure 4. Vertical slice AA′ through the seismic amplitude volume. Some faults show offsets (such as that indicated by the purple arrows) at the top of the basement (the blue horizon) but appear as flexures in the sedimentary section (indicated by the blue arrows). The top Hunton (the yellow horizon) and top Woodford (the red horizon) form the bottom of the exploration target for most operators. The orange arrows indicate a possible fault given its offset deeper in the section (the pink arrow); however, because of the lack of displacement, many faults do not appear on the horizon slices through the coherence volume at the (b) top basement or (c) top Hunton. The boxes with a black outline and a white fill in the coherence are the data cutouts (the seismic data are courtesy of TGS).

proves the continuity of some of the lineaments imaged by curvature, and it also delineates other features that correlate with the paleotopographic features on the top Hunton (Figure 6d). We attribute some of the greater detail seen along the top Hunton to the higher frequency data at the shallower depths compared to the lower frequencies at the deeper basement. However, some of these features are geologic, perhaps related to the helicoidal deformation of strike-slip faults such as those observed over a Trenton Limestone play in Ohio (Sagan and Hart, 2006). In total, 56, 74, and 85 lineaments were mapped on the coherence, curvature, and aberrancy, respectively, along the top Hunton (Figure 6f). Coherence reveals a higher number of features on the top Hunton than the top of the basement but still less than revealed by curvature and aberrancy. Aberrancy reveals the highest number of lineaments on the top Hunton.

Because the Woodford Formation overlays the Hunton, aberrancy delineates similar features on the top Hunton and top Woodford (Figure 6d and 6e). Hence, we do not show a separate analysis for the Woodford and anticipate a similar statistical correlation. The earthquakes in the STACK area do not occur isolated but rather correlate with the lineaments delineated by the curvature and aberrancy (Figures 5b, 5c, and 6c–6e). Aberrancy provides superior imaging of these structural features on the top Hunton and top basement. Where earthquakes align with aberrancy anomalies, they corroborate our hypothesis that these anomalies are faults or fault zones with offsets that fall below the seismic resolution, or even weaker, fractured flexures rather than simple flexures that have deformed elastically or plastically.

On vertical slices (e.g., see Figures 3c, 3f, and 4a), these lineaments represent subvertical discontinuity surfaces that vertically offset and/or otherwise deform the stratigraphic reflectors. However, we also do not observe the thickening of the stratigraphic packages toward the faults in the downthrown sides of the faults. Along any of the discontinuity surfaces, we observe that offset geometries are often localized on the deeper reflectors, whereas the flexures often occur upsection on the shallower reflectors (e.g., Figure 4a). Because the vertical seismic resolution decreases (and the loss of lateral resolution resulting in blurring increases) with depth, this observation implies that the change in the fault character with depth is based on geology rather than on seismic data quality. We also observe that many of the discontinuities extend into the basement and offset or truncate vertically stacked intrabasement reflectors interpreted by Chopra et al. (2017) and Kolawole et al. (2020) to be igneous sills (e.g., Figure 4a). Although sills can step upward (Chopra et al., 2017), such steps always follow a zone of weakness, which we would also interpret to be joint or fault. Following on the observations from previous studies (Chopra et al., 2017; Kolawole et al., 2019; Patel and Marfurt, 2019) and observing a correlation between the earthquakes and lineaments delineated by curvature and aberrancy, we interpret these illuminated lineaments as faults. Overall, these fault-related lineaments show little to no offset on the top basement and top Hunton surfaces. Within the seismic survey, the largest observed

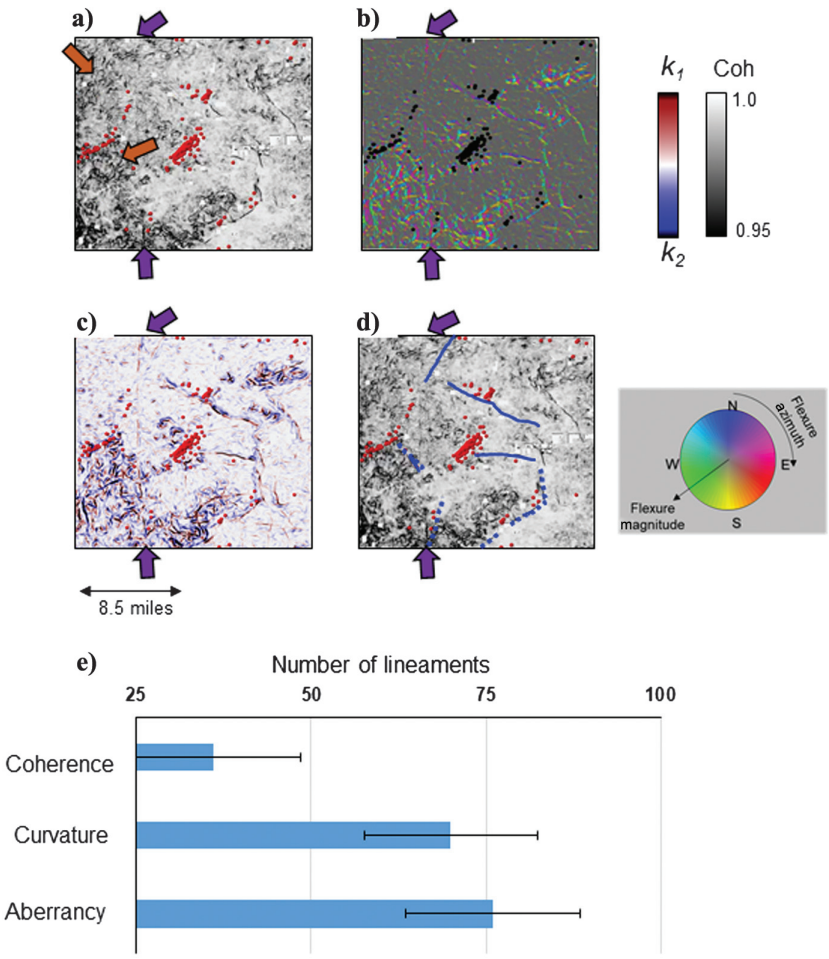

Figure 5. Horizon slices along top basement through the (a) band-limited multispectral coherence (30–55 Hz), (b) corendered aberrancy magnitude and azimuth volumes, and (c) corendered k_1 and k_2 curvature. Earthquake locations are indicated as red or black dots. (d) The same horizon slice is shown in (a) but now with seismogenic faults mapped by curvature and aberrancy marked as blue lines. Seismogenic faults that are better mapped by aberrancy appear as dashed blue lines. The purple arrow indicates the north–south strike-slip El Reno fault, which is poorly imaged by coherence but is well imaged by curvature and aberrancy. The orange arrow points to paleotopographic features on the top basement. (e) Statistical analysis of the number of faults mapped on (a-c). Earthquake locations from the OGS catalog (the seismic data are courtesy of TGS).

offset of faulting at the top basement surface is approximately 30 ms, whereas, at the top Hunton, the largest observed flexure is approximately 45 ms.Figure3

Distribution of interpreted fault lineaments

By integrating the seismic attribute maps (Figures 5 and 6), we identified and mapped 86 fault lineaments on the top basement, 88 on the top Hunton, and 90 on the top Woodford surfaces (Figure 7a). Essentially, the density of fault lineaments decreases slightly with depth from the sedimentary sequences into the basement. The frequency-azimuth distribution of the fault lineaments for all three surfaces shows multimodal distribution with similar prominent trends (Figure 7b–7d). The prominent trends on three surfaces are north-northwest–south-southeast to approximately north–south, northwest–southeast, and northeast–southwest. Among the northwest and northeast trends, the northwest trend appears to be more dominant on the top basement and top Woodford surfaces.

Relocated earthquake patterns and focal mechanism solutions

For the Kingfisher-Blaine-Canadian counties (Figure 1a and 1e), we relocated a total of 3523 recorded between 2010 and 2019 with magnitudes ranging from Mw 0.6 to Mw 4.5 (Figure 8a and 8b). The median error in the relocated events was 400 m horizontally and 800 m vertically. HypoDD relocation can get excellent relative locations, but the absolute event location depends on the velocity model. This is a challenge for the regional seismic network. The surface locations (lat, long) of these events are generally more reliable than depth. The event histogram (Figure 8a) shows that although events extend down to >12 km depths, most of the earthquakes in this part of the basin occurred between 4 and 8 km, which is located within the crystalline basement (Figure 8a). Only 2.2% of the events were located in the sedimentary formations. Additionally, a scatterplot of the earthquake magnitude shows that most intrasedimentary earthquakes cover a relatively narrower range (Mw1.9–2.8) compared to those hosted within the basement (Mw1.0–3.8).

A north–south vertical section of seismicity clusters across the study area (Figure 8b) shows that the event clusters delineate subvertical rupture planes that extend from the deep basement zones (>10 km) across the top basement surface through the shallow sedimentary sequences. Additionally, the temporal evolution of the seismicity shows that the events recorded from 2015 onward overprint the older event clusters in the basement. Further, the shallowest events (the blue arrow in Figure 8b) occurred more recently, consistent with the period of the most prevalent seismicity in the study area (Figure 1c).

We generated focal mechanism solutions for 20 events across the study area (Figure 9 and 9b). In plane view, the relocated event clusters and focal mechanism solutions are collocated with (occurred directly on or near) several fault lineaments in the seismic attribute maps of the top basement (Figure 9a and 9b). Overall, the focal mechanism solutions show predominantly strike-slip faulting with minor normal faulting along

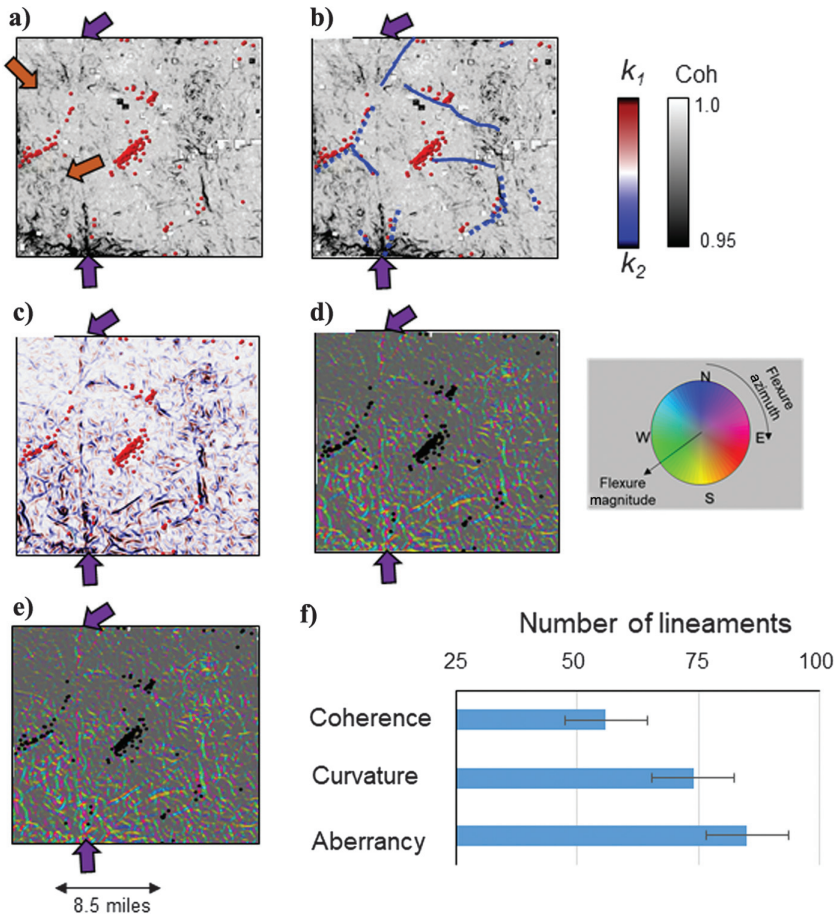

Figure 6. Horizon slices along the top Hunton through the (a) band-limited multispectral coherence (30–55 Hz), (c) corendered k_1 and k_2 curvature, and (d) corendered aberrancy magnitude and azimuth volumes. (b) The same horizon slice is shown in (a) but now with seismogenic faults mapped by curvature (the dark blues lines) and aberrancy (the blue dashed lines). The purple arrow indicates the same north–south strike-slip El Reno fault as in Figure 5. The orange arrow points to the same location as Figure 5a, indicating a decrease in the paleotopographic feature's signature on Hunton. Hunton's seismic attributes delineate several other structural features on Hunton that do not appear on top of the basement. (e) Horizon slice along the top Woodford through the corendered aberrancy magnitude and azimuth volumes. Note that there is little change from the top Hunton shown in (c). (f) Statistical analysis of the number of faults mapped on (a-c). The red and black earthquake locations from the OGS catalog (the seismic data are courtesy of TGS).

northwest–southeast and northeast–southwest-trending nodal planes. The overlay of earthquake events on the seismic depth-sections (e.g., Figure 10a and 10b) shows the collocation of basement and sedimentary earthquake clusters with stacked discontinuity surfaces. Extracted curvature seismic attributes reveal multiple subvertical discontinuity surfaces that extend from the basement up into the sedimentary cover and connect isolated or clusters of earthquake events in basement and sedimentary intervals (Figure 10b and 10c).

Discussion

Seismic illumination of small-offset seismogenic faults with aberrancy and curvature attributes

The band-limited multispectral coherence (Figure 5a) provides a much better improvement to broadband coherence (Figure 4a). However, the lateral extents of the fault lineaments in the coherence maps are largely underrepresented when compared to the curvature (Figure 5c) and aberrancy (Figure 5b) maps. For example, aberrancy and curvature attributes show a significant improvement in delineating the north–south-trending faults compared to coherence. Additionally, we observe that the coherence fault lineaments are restricted to fault segments that show a distinct offset character with the associated significant flexure of the stratigraphic reflectors. Coherence measures similarity between neighboring waveforms. If the waveforms are very similar, the coherence attribute will have a high value, and if the waveforms are very different, coherence will have a low value. Coherence will image a fault with a seismically resolvable offset (more than one-quarter of the seismic wavelength) because the waveforms across the faults will be dissimilar. Figure 4b and 4c shows broadband coherence computed on the seismic data and extracted across the top of the basement and Hunton Formation. Some of the faults have seismically resolvable offset on the top of the basement (Figure 4b). Coherence fails to image these faults in the sedimentary sections because flexures in the sedimentary section cause waveform similarity in nearby traces (Figure 4c).

Studies have shown that outboard of the Nemaha Fault (Figure 1a), the faults generally show small (maximum of 120 m) vertical separation of stratigraphic surfaces (Firkins et al., 2020; Kolawole et al., 2020). Since fault vertical separation generally includes both the ductile (stratigraphic flexure) and brittle (fault throw) components of the fault deformation, the estimate suggests that the fault throws will be generally less than 120 m. Therefore, we infer that in geologic settings such as the Anadarko Shelf, where such low fault throws dominate, the curvature and aberrancy seismic attributes may be the most effective attribute in illuminating fault traces. Essentially, the aberrancy and curvature attributes may be additionally effective in delineating fault zones with subseismic offsets. In contrast, the coherence attribute may be more useful where the fault offset is significant enough to be seismically resolvable. However, we find that an interpretation approach that incorporates all three attributes best illuminates the lateral extents of the mapped fault (e.g., Figure 6b). Although previous structural investigations in the Anadarko Basin used curvature and coherence attributes to delineate fault segments (Elebiju et al., 2011; Liao et al., 2017; Kolawole et al., 2019, 2020), we emphasize that the aberrancy seismic attribute provides even better detail of structural deformation in such geologic settings as the study area (Patel and Marfurt, 2019; Verma and Bhattacharya, 2019).

Our results show that several faults in the study area extend from the sedimentary cover into the basement (e.g., Figures 3c, 3f, 8b, 10b, and 10c). Consistent with observations in Kolawole et al. (2020), we do not observe growth sequences in the downthrown blocks of the faults, thus indicating that the illumi-

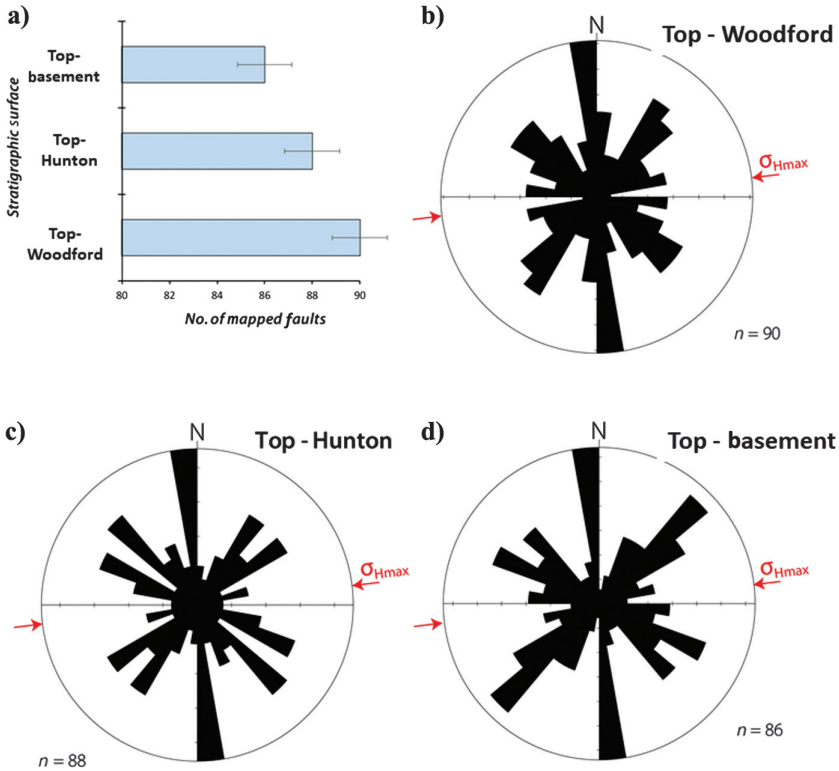

Figure 7. (a) Histogram of interpreted faults for the three stratigraphic surfaces mapped in this study. Frequency-azimuth rose diagrams of the mapped fault segments for (b) top Woodford, (c) top Hunton, and (d) top basement showing dominant trends along north–south, northwest–southeast, and northeast–southwest. The red arrows represent the σ_{Hmax} (maximum horizontal stress) orientation for the study area found by Qin et al. (2019).

nated fault deformation in the analyzed stratigraphic interval (Basement to Woodford) is postdepositional. A detailed analysis of the vertical partitioning of structural styles along the basement-rooted faults in the Anadarko Basin was presented in Kolawole et al. (2020). It was shown that the faults are transpressional faults with an upward propagation that features a deeper domain of faulted blocks near the top basement, which transitions into the faulted monocline upsection and simple monoclinal flexures in the shallower sections. Therefore, the small vertical offset of these faults provides an explanation for the rare occurrence of fault offsets only in the near top basement depths and the dominance of the monoclinal flexures across most of the sedimentary section (e.g., Figure 4a). Additionally, the relatively more compliant mechanical properties of the sedimentary units make it easier for the faults and top basement paleotopographic features to flexurally deform the rocks. Hence, faults show better lateral continuity on Hunton and Woodford than on the top of the basement. Therefore, we propose that the large-scale structural styles of these small-offset faults make the aberrancy and curvature (flexure illuminating) seismic attributes the ideal attributes for their illumination.

In the plane view (e.g., Figures 5, 6, and 9) and cross section (Figure 10a–10c), the distribution of relocated seismicity clusters shows a collocation of the earthquakes with our carefully illuminated fault lineaments. Thus, we recommend the use of aberrancy and curvature seismic attributes for the investigation of potentially seismogenic faults in the Anadarko Basin and other intraplate sedimentary basins, where small-offset preexisting faults pose critical seismic hazards. In relation to the recent spike in induced seismicity in Oklahoma and surrounding areas (e.g., Figure 1a), the seismogenic basement-rooted faults are often delineated after the fact (Chen et al., 2017; Schoenball and Ellsworth, 2017; Kolawole et al., 2019). There are several fault lineaments in the survey along or in the vicinity of which no earthquake activities have been recorded (e.g., Figure 6d). However, we suggest that the careful integration of fault geometry mapping (using the recommended seismic attributes) with geomechani-

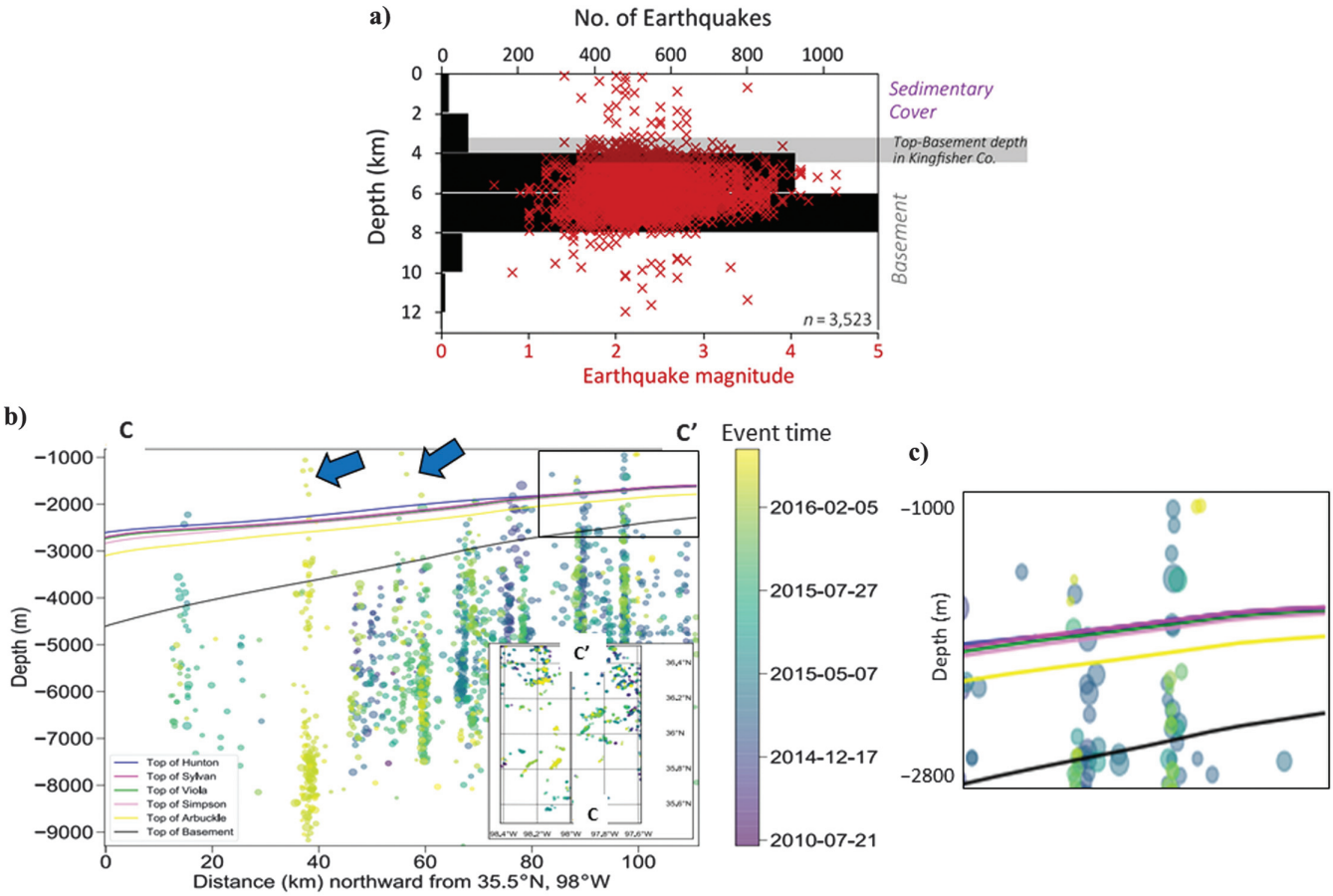

Figure 8. (a) Histogram of the depth distribution of the relocated earthquakes in the study area overlaid with the depth-distribution of earthquake magnitude. (b) North–south vertical section across the study area shows the temporal evolution of the seismicity and the subvertical geometries of the earthquake clusters. The blue arrows point to recently occurred earthquakes in the sedimentary section. The horizons (from bottom to top) are the top basement (in black), top Arbuckle (in yellow), top Simpson (in pink), top Viola (in green), top Sylvan (in dark pink), and top Hunton (blue). The top basement surface (the black line) is from Crain and Chang (2018). (c) A magnified view of the black rectangle in (b) showing that the thickness of the formations decreases in the north–northeast direction (the earthquake data are courtesy of OGS).

cal modeling of fault reactivation potential (Walsh and Zoback, 2016; Qin et al., 2019) of the mapped faults may be effective in mitigating resource-exploration-related seismic triggering.

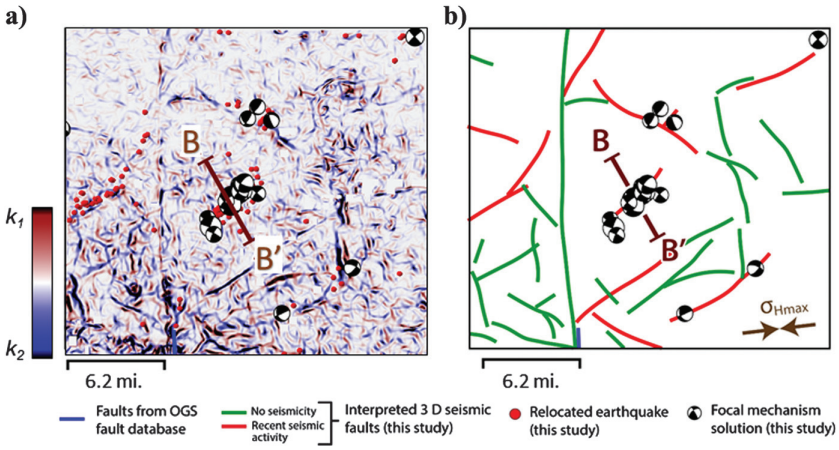

Figure 9. (a) Horizon slice along the top Hunton through the corendered k_1 and k_2 curvature volumes overlaid with seismicity epicenters, focal mechanism solutions, and previously reported fault segments in the area (the blue line). (b) Interpretation of the illuminated fault lineaments in Figure 9a. The red and green lines are the interpreted faults from (a), and the blue lines show the faults from OGS. The brown arrows represent the σ_{Hmax} orientation for the study area computed by Qin et al. (2019) (the seismic data are courtesy of TGS, and the earthquake data are courtesy of OGS).

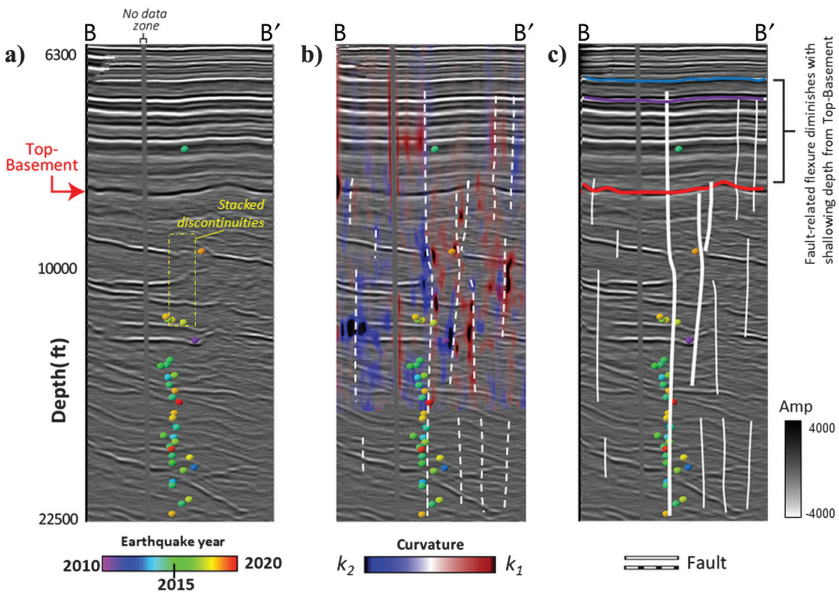

Figure 10. Vertical slice through the depth-converted (a) seismic amplitude volume along line BB′ through the northwest-trending earthquake cluster shown in Figure 9. The red, purple, and blue lines represent top basement, top Hunton, and top Meramec. (b) Line BB′ through corendered amplitude and k_1 and k_2 curvature volumes. The vertical anomaly adjacent to the no-permit zone is an artifact. (c) Interpreted faults on line BB′ using flexures mapped by the curvature and discontinuities seen in the seismic amplitude data. The reflectors in the basement are from intruded sills, some of which are faulted (Chopra et al., 2017; Kolawole et al., 2020) (the seismic data are courtesy of TGS).

The illuminated fault structure and induced seismicity in Central Oklahoma and other areas

The illuminated faults show dominant plan-view trends along the north–south, northwest–southeast, and northeast–southwest orientations (Figure 7b–7d). The focal mechanism solutions for the events show a predominance of strike-slip with minor normal fault reactivation on northwest- and northeast-trending nodal planes (Figure 9a and 9b). Kolawole et al. (2019) demonstrate that the Precambrian crystalline basement's structural fabric underlying Oklahoma, Kansas, and the surrounding areas is defined by a prominent northeast- and northwest-trending fault and fracture networks with a minor north–south-trending set. Kolawole et al. (2020) show that these Precambrian structural trends were reactivated in the Late Paleozoic, leading to basement-driven (unidirectional) and intrasedimentary-driven (bidirectional) fault propagation patterns across the Anadarko Shelf. However, Qin et al. (2019) show that these three structural trends were reactivated in varying proportions relative to one another in various parts of the basin. In some places, only one or more of the structural trends propagated up into the pre-Paleozoic cover. Here, we observe a dominance of all three structural trends, extending across the basement-sedimentary interface (Figures 7b, 7c, and 10a–10c). The north–south structural trend is parallel to the trend of the Nemaha Fault Zone (Figure 1a). The pervasiveness of the trend in the sedimentary units most likely represents the influence of the proximity of the area to the Nemaha Fault Zone. This interpretation is consistent with a recent regional-scale structural analysis in northern Oklahoma that demonstrated that proximal to the Nemaha Fault Zone, north–south-trending structural deformation is relatively more pervasive, north–south faults are longer, and that there is a higher likelihood of the basement-rooted faults to extend further up into the shallower sedimentary units (Firkins et al., 2020). Kolawole et al. (2020) derive a quantitative relationship between fault offsets at a deeper depth and the amplitudes of flexure with decreasing depth, and they show that the basement-driven fault segments (i.e., basement-rooted) propagate further up-section into the Pennsylvanian units than those that were intrasedimentarily driven (i.e., not base-

ment-rooted). It was also shown that the larger the offset was on a basement-rooted fault, the shallower were the reaches of the flexural deformation associated with the fault. Therefore, based on the inferred Late Paleozoic timing of deformation and the conditions that promote vertical propagation of faulting and flexure into the shallower depths, we speculate that the reservoir stratigraphic packages in the shallower Pennsylvanian units will most likely be influenced by the large-offset basement-rooted faults. Although this hypothesis is interesting, it is not the primary focus of this study.

Qin et al. (2019) perform a detailed analysis of the stress distributions in Oklahoma and find that the average orientation for maximum horizontal stress (σ_{Hmax}) is approximately 85°, ranging between 80° and 90°. Based on the Coulomb failure criterion, the optimal fault orientation would be approximately 60° or 120° strike, which is consistent with the observed seismogenic fault orientations in the crystalline basement. The focal mechanism solutions and fault orientations for the seismogenic faults in the study region are also consistent with the overall trend from Oklahoma, suggesting that earthquakes tend to occur along optimally oriented structures (Figure 9). The normal faulting events may be associated with flower structures along the strike-slip faults, as observed in the Woodward sequence located farther northwest of the study area (Qin et al., 2018). Previous studies have shown how fault orientations with respect to the ambient stress field influence the susceptibility of fault segments to shear reactivation, which may be seismogenic or aseismic (Walsh and Zoback, 2016; Alt and Zoback, 2017; Kolawole et al., 2019; Qin et al., 2019). Based on the orientation of maximum horizontal stress in the Kingfisher County area (the approximately 83° red arrows in Figure 7b–7d; Qin et al., 2019), we infer that the northwest–southeast- and northeast–southwest-trending fault segments are most critically oriented for shear reactivation in the present-day stress field. Thus, it is not surprising that the illuminated fault lineaments with earthquakes on them (Figures 8b, 9a, and 9b) are oriented at low oblique angles to the stress field. Some lineaments hosted seismicity that occurred during hydraulic fracturing completions. There are other lineaments that are otherwise favorably oriented for failure yet remain quiescent because there were no hydraulic fracturing completions close enough to those faults to increase the shear stress past a failure threshold. It is most likely the case that faults that fail during hydraulic fracturing are critically stressed before completion. However, the absolute magnitude of stress on faults before operations is likely unknowable.

Figure 7 shows a peak of north–south-oriented faults in the study region interpreted from seismic imaging, and Figure 9b shows some identified lineaments on seismic attributes. The north–south orientation has also been identified from well logs in central Oklahoma (Holland, 2013b) and mapped faults from the OGS database (Qin et al., 2019). Several recent studies using 3D seismic data revealed basement-rooted north–south faults, which likely represent reactivation and propagation of the Precambrian basement structural trends into the sedimentary cover (Kolawole et al., 2019). However, these faults are not optimally oriented for fault slip in the regional stress regime inferred by Qin et al. (2019); the east–west-trending maximum horizontal stress direction would act to increase the normal stress on a north–south-trending fault. Coulomb failure criterion suggests that north–south-oriented faults would require much higher pore-fluid pressure to reactivate under the average background stress field with σ_{Hmax} approximately 85°, which could explain the discrepancy between seismogenic faults and interpreted faults from structural interpretation.

As described above, the interpreted faults are basement-rooted strike-slip faults that developed during the Late Paleozoic transpressional tectonics (Gay, 2003; Liao et al., 2017; Kolawole et al., 2020), and the vertical partitioning of their structural styles (Kolawole et al., 2020) facilitates a prevalence of flexures along most of their segments (e.g., Figures 4a and 10a–10c). These flexures may be simple differential compaction folds, faults smeared by seismic processing, subseismic conjugate faults, or folds associated with reactivated basement faults. Patel and Marfurt (2019) hypothesize that some flexures are due to differential compaction caused by top basement paleotopography.

The seismicity recorded within the study area (Figure 8a and 8b) may be related to fault reactivation by wastewater disposal into the deeper sedimentary units (e.g., the Arbuckle Formation), hydraulic fracturing within shallower sedimentary units (e.g., the Woodford and Hunton Formations), or natural intraplate fault reactivation. The vertical extents of the seismic events (Figure 8b) and collocation with fault discontinuities in the 3D seismic data (Figure 10a–10c) may indicate a potential link between intrasedimentary and basement-hosted seismicity in this part of the Anadarko Basin. Therefore, the analyses presented in this study may provide better insight into the structures in the area relevant for future exploration activities in the area.

Conclusion

In this paper, we have used attributes computed on a subset of 1100 sq mi of seismic reflection data to delineate the tectonic framework of the STACK area of the Anadarko Basin. The attributes reveal that the faults in the area extend from sedimentary cover into the basement with the rare occurrence of offsets near the top basement but the prevalence of flexures across the sedimentary section. We show that, although the broadband coherence delineated some of the faults near the basement, it fails to image them in the sedimentary section due to the subseismic vertical offset of the faults. Because of layering, the empirical analysis showed that faults are tuned at a 30–55 Hz frequency in the Mississippian formations. Hence, we suggest limiting the multispectral coherence to the bandwidth that best

represents the discontinuities of interest. The lateral and horizontal continuity of the fault is best delineated by flexure-sensitive attributes such as curvature and aberrancy. Unlike coherence, curvature and aberrancy map smoothly deformed rather than discontinuous structural features. We demonstrate that the location of the fault is best delineated by the combination of band-limited multispectral coherence, aberrancy, and curvature. Aberrancy delineates the greatest number of fault lineaments, and we consider it the most effective attribute to delineate tectonic features in geologic settings such as the Anadarko Basin. The lineament analysis of the seismic attributes shows that the density of fault lineaments decreases from sedimentary layers to the top basement. The illuminated faults show multimodal distribution with dominant plan-view trends along the north–south, northwest–southeast, and northeast–southwest.

The locally recorded earthquakes collocate near the fault lineaments delineated by the seismic attributes indicating the seismogenic nature of the faults in the Anadarko Basin. The earthquake cluster reveals a subvertical rupture plane extending from the sedimentary section to the deep basement. The earthquakes' focal mechanism reveals predominantly strike-slip faulting with minor normal faulting along northwest- and northeast-trending nodal planes. Some of the recent earthquake events occurred in the sedimentary section coinciding with the increase in oil and gas exploration and production activities in the region. Several faults in the STACK area are imaged by the seismic attributes shown in this study, but no earthquake activity has been recorded in their vicinity. We also recommend using flexure-sensitive attributes to delineate structural features in other basins with structural styles that are similar to those of the Anadarko Basin.

Acknowledgments

We thank TGS for providing a license to the Kingfisher/Loyal 3D seismic reflection data used in this study. We thank OGS for providing the earthquake data used in this study. The first author wishes to thank Marathon Oil for financial support during the last two years of his Ph.D. studies, devoted to studying the Meramec Formation of the STACK play.

Data and materials availability

Data associated with this research are confidential and cannot be released.

Appendix A

Seismic attributes computation basics

Here, we summarize the mathematical details on computing the curvature and aberrancy. A detailed explanation of the curvature computation can be found in Chopra and Marfurt (2007). Qi and Marfurt (2018) and Gao and Di (2014) provide a detailed description of the aberrancy computation.

Curvature

Mathematically, the first step in curvature computation fits a quadratic surface $z(x,y)$ to an interpreted horizon (Chopra and Marfurt, 2007):

$$z(x,y) = ax^2 + cxy + by^2 + dx + ey + f. \tag{A-1}$$

Once the coefficients (a, b, c, d, e, and f) are estimated, the mean of the curvature (k_{mean}) and Gaussian curvature (k_{Gauss}) is calculated are

$$K_{\text{mean}} = [a(1+e^2) + b(1+d^2) - cde]/(1+d^2+e^2)^{3/2} \tag{A-2}$$

$$k_{\text{Gauss}} = (4ab - c^2)/(1+d^2+e^2)^2. \tag{A-3}$$

The principal curvature (k_1 and k_2) can be calculated using k_{mean} and k_{Gauss},

$$k_1 = k_{\text{mean}} + (k_{\text{mean}}^2 - k_{\text{Gauss}})^{1/2} \tag{A-4}$$

$$k_2 = k_{\text{mean}} - (k_{\text{mean}}^2 - k_{\text{Gauss}})^{1/2}, \tag{A-5}$$

where k_1 is the most-positive curvature and k_2 is the most-negative curvature.

Aberrancy

Gao and Di's (2014) aberrancy computation method requires derivatives of the dip vector in a coordinate system to be rotated to align with the local reflector dip and azimuth. Once we have computed the second derivative of the dip vector in the rotated coordinate system, the apparent flexure $f(\psi)$ at azimuth ψ is given by

$$f(\psi) = \frac{\partial^3 z'}{\partial x'^3}\cos^3\psi + 3\frac{\partial^3 z'}{\partial x'^2 \partial y'}\cos^2\psi\,\sin\psi + 3\frac{\partial^3 z'}{\partial x' \partial y'^2}\cos\psi\sin^2\psi + \frac{\partial^3 z'}{\partial y'^3}\sin^3\psi, \tag{A-6}$$

where x', y', and z' are the rotating axis. The aberrancy is calculated by finding the extrema of equation A-6. The extrema are the roots of equation A-7:

$$\frac{df(\psi)}{d\psi} = 3\cos^3\psi\left[-\frac{\partial^3 z'}{\partial x' \partial y'^2}\tan^3\psi - \left(2\frac{\partial^3 z'}{\partial x'^2 \partial y'} - \frac{\partial^3 z'}{\partial y'^3}\right) \times \tan^2\psi + \left(2\frac{\partial^3 z'}{\partial x' \partial y'^2} - \frac{\partial^3 z'}{\partial x'^3}\right)\tan\psi + \frac{\partial^3 z'}{\partial x'^2 \partial y'}\right] = 0. \tag{A-7}$$

Equation A-7 is cubic in terms of $\tan\psi$; hence, it has three roots. The magnitude of the aberrancy is the sum

of these three roots, and the azimuth of the aberrancy is given by ψ.

References

Alt, R. C., and M. D. Zoback, 2017, In situ stress and active faulting in Oklahoma in situ stress and active faulting in Oklahoma: Bulletin of the Seismological Society of America, **107**, 216–228, doi: 10.1785/0120160156.

Burke, K., 1977, Aulacogens and continental breakup: Annual Review of Earth and Planetary Sciences, **5**, 371–396, doi: 10.1146/annurev.ea.05.050177.002103.

Chen, X., N. Nakata, C. Pennington, J. Haffener, J. C. Chang, X. He, Z. Zhan, S. Ni, and J. I. Walter, 2017, The Pawnee earthquake as a result of the interplay among injection, faults and foreshocks: Scientific Reports, **7**, 4945, doi: 10.1038/s41598-017-04992-z.

Chopra, S., L. Infante-Paez, and K. J. Marfurt, 2017, Intrabasement intrusions in the STACK area of Oklahoma: AAPG Explorer, 42229.

Chopra, S., and K. J. Marfurt, 2007, Seismic attributes for prospect identification and reservoir characterization: SEG.

Crain, K. D., and J. C. Chang, 2018, Elevation map of the top of the crystalline basement in Oklahoma and surrounding states: Oklahoma Geological Survey. Open-File Rept. OF1-2018.

Elebiju, O. O., S. Matson, G. R. Keller, and K. J. Marfurt, 2011, Integrated geophysical studies of the basement structures, the Mississippi chert, and the Arbuckle Group of Osage County region, Oklahoma: AAPG Bulletin, **95**, 371–393, doi: 10.1306/08241009154.

Ellsworth, W. L., 2013, Injection-induced earthquakes: Science, **341**, 1225942, doi: 10.1126/science.1225942.

Eyre, T. S., D. W. Eaton, M. Zecevic, D. D'Amico, and D. Kolos, 2019, Microseismicity reveals fault activation before Mw 4.1 hydraulic-fracturing induced earthquake: Geophysical Journal International, **218**, 534–546, doi: 10.1093/gji/ggz168.

Firkins, M., F. Kolawole, K. J. Marfurt, and B.M. Carpenter, 2020, Attribute assisted characterization of basement faulting and the associated sedimentary sequence deformation in north-central Oklahoma: Interpretation, **8**, no. 4, SP175–SP189, doi: 10.1190/INT-2020-0053.1.

Gao, D., 2013, Wavelet spectral probe for seismic structure interpretation and fracture characterization: a workflow with case studies: Geophysics, **78**, no. 5, O57–O67, doi: 10.1190/geo2012-0427.1.

Gao, D., and H. Di, 2014, Extreme curvature and extreme flexure analysis for fracture characterization from 3D seismic data: New analytical algorithms and geologic implications: Geophysics, **80**, no. 2, IM11–IM20, doi: 10.1190/geo2014-0185.1.

Gay, S. P., Jr, 2003, The Nemaha trend-a system of compressional thrust-fold, strike-slip structural features in Kansas and Oklahoma (part 2, conclusion): The Shale Shaker, **54**, 39–49.

Hardebeck, J. L., and P. M. Shearer, 2002, A new method for determining first-motion focal mechanisms: Bulletin of the Seismological Society of America, **92**, 2264–2276, doi: 10.1785/0120010200.

Holland, A. A., 2013a, Earthquakes triggered by hydraulic fracturing in south-central Oklahoma: Bulletin of the Seismological Society of America, **103**, 1784–1792, doi: 10.1785/0120120109.

Holland, A. A., 2013b, Optimal fault orientations within Oklahoma: Seismological Research Letters, **84**, 876–890, doi: 10.1785/0220120153.

Holloway, S., A. Holland, and G. Keller, 2015, Industry contributions to the Oklahoma fault database: Mid-Continent Section.

Johnson, K., 2008, Geologic history of Oklahoma: Educational Publication, **9**, 3–8.

Johnson, K. S., and B. J. Cardott, 1992, Geologic framework and hydrocarbon source rocks of Oklahoma: Source Rocks in the Southern Midcontinent, 1990 Symposium, Oklahoma Geological Survey Circular, **93**, 21–37.

Kaven, J. O., S. H. Hickman, A. F. McGarr, and W. L. Ellsworth, 2015, Surface monitoring of microseismicity at the Decatur, Illinois, CO2 sequestration demonstration site: Seismological Research Letters, **86**, 1096–1101, doi: 10.1785/0220150062.

Kolawole, F., C. Johnson, J. C. Chang, K. J. Marfurt, D. A. Lockner, Z. Reches, and B. M. Carpenter, 2019, Oklahoma's basement: Primed for seismic reactivation: Nature Geoscience, in revision.

Kolawole, F., M. T. Simpson, and B. M. Carpenter, 2020, Basement-controlled deformation of sedimentary sequences, Anadarko Shelf, Oklahoma: Basin Research, **32**, 1365–1387, doi: 10.1111/bre.12433.

Langenbruch, C., M. Weingarten, and M. D. Zoback, 2018, Physics-based forecasting of man-made earthquake hazards in Oklahoma and Kansas: Nature Communications, **9**, 1–10, doi: 10.1038/s41467-018-06167-4.

Lei, X., D. Huang, J. Su, G. Jiang, X. Wang, H. Wang, X. Guo, and H. Fu, 2017, Fault reactivation and earthquakes with magnitudes of up to Mw4.7 induced by shale-gas hydraulic fracturing in Sichuan Basin, China: Scientific Reports, **7**, 7971, doi: 10.1038/s41598-017-08557-y.

Li, F., J. Qi, B. Lyu, and K. J. Marfurt, 2018, Multispectral coherence: Interpretation, **6**, no. 1, T61–T69, doi: 10.1190/INT-2017-0112.1.

Liao, Z., H. Liu, Z. Jiang, K. J. Marfurt, and Z. E. Reches, 2017, Fault damage zone at subsurface: A case study using 3D seismic attributes and a clay model analog for the Anadarko Basin, Oklahoma: Interpretation, **5**, no. 2, T143–T150, doi: 10.1190/INT-2016-0033.1.

Machado, G. L., G. J. Hickman, M. P. Gogri, K. J. Marfurt, M. J. Pranter, and Z. A. Reza, 2019, Characterization of Arbuckle-basement wastewater disposal system, Payne County, Northern Oklahoma: Interpretation, **7**, no. 4, SL19–SL36, doi: 10.1190/INT-2019-0025.1.

Marsh, S., and A. Holland, 2016, Comprehensive fault database and interpretive fault map of Oklahoma: Oklahoma Geological Survey. Open-File Rep. OF2-2016.
McBee, W., 2003, The Nemaha and other strike-slip faults in the midcontinent USA: AAPG Mid-Continent Section Meeting Proceedings, 1–23.
National Research Council, 2013, Induced seismicity potential in energy technologies: National Academies Press, 31–48.
Oklahoma Geological Survey, 1965, Earthquake catalog, https://ogsweb.ou.edu/eq_catalog/, data set accessed 19 January 2020.
Partyka, G., J. Gridley, and J. A. Lopez, 1999, Interpretational applications of spectral decomposition in reservoir characterization: The Leading Edge, **18**, 353–360, doi: 10.1190/1.1438295.
Patel, S., and K. J. Marfurt, 2019, Flexures in the Anadarko Basin: Do they indicate faulting or folding? 89th Annual International Meeting, SEG, Expanded Abstracts, 1953–1957, doi: 10.1190/segam2019-3216621.1.
Perry, W. J., 1989, Tectonic evolution of the Anadarko Basin region, Oklahoma: U.S. Geological Survey Bulletin, 1866.
Peyton, L., R. Bottjer, and G. Partyka, 1998, Interpretation of incised valleys using new-3D seismic techniques: A case history using spectral decomposition and coherency: The Leading Edge, **17**, 1294–1298, doi: 10.1190/1.1438127.
Qi, X., and K. J. Marfurt, 2018, Volumetric aberrancy to map subtle faults and flexures: Interpretation, **6**, no. 2, T349–T365, doi: 10.1190/INT-2017-0114.1.
Qin, Y., X. Chen, B. M. Carpenter, and F. Kolawole, 2018, Coulomb stress transfer influences fault reactivation in areas of wastewater injection: Geophysical Research Letters, **45**, 11059–11067, doi: 10.1029/2018GL079713.
Qin, Y., X. Chen, J. I. Walter, J. Haffener, D. T. Trugman, B. M. Carpenter, M. Weingarten, and F. Kolawole, 2019, Deciphering the stress state of seismogenic faults in Oklahoma and southern Kansas based on an improved stress map: Journal of Geophysical Research, Solid Earth, **124**, 12920–12934, doi: 10.1029/2019JB018377.
Sagan, J. A., and B. S. Hart, 2006, Three-dimensional seismic-based definition of fault-related porosity development: Trenton–Black River interval, Saybrook, Ohio: AAPG Bulletin, **90**, 1763–1785, doi: 10.1306/07190605027.
Schmidt, I., M. Docherty, F. Pauget, and S. Lacaze, 2010, Improved 3D seismic interpretation and reservoir model construction using PaleoScan technology: AAPG, Expanded Abstract.
Schoenball, M., and W. L. Ellsworth, 2017, Waveform-relocated earthquake catalog for Oklahoma and southern Kansas illuminates the regional fault network: Seismological Research Letters, **88**, 1252–1258, doi: 10.1785/0220170083.
Shemeta, J. E., B. C. Edward, and L. C. Clifford, 2019, Well stimulation seismicity in Oklahoma: Cataloging earthquakes related to hydraulic fracturing: Asia Pacific Unconventional Resources Technology Conference, 95–106.
Skoumal, R. J., M. R. Brudzinski, and B. S. Currie, 2015, Earthquakes induced by hydraulic fracturing in Poland Township, Ohio: Bulletin of the Seismological Society of America, **105**, 189–197, doi: 10.1785/0120140168.
Skoumal, R. J., R. Rosamiel, M. R. Brudzinski, A. J. Barbour, and B. S. Currie, 2018, Earthquakes induced by hydraulic fracturing are pervasive in Oklahoma: Journal of Geophysical Research, **123**, 10918–10935, doi: 10.1029/2018JB016790.
Verma, S., and S. Bhattacharya, 2019, Delineation of complex fault network North Slope, Alaska using seismic attributes: 89th Annual International Meeting, SEG, Expanded Abstracts, 1893–1897, doi: 10.1190/segam2019-3214607.1.
Waldhauser, F., and W. L. Ellsworth, 2000, A double-difference earthquake location algorithm: Method and application to the northern Hayward fault: Bulletin of the Seismological Society of America, **90**, 1353–1368, doi: 10.1785/0120000006.
Walsh, F. R., and M. D. Zoback, 2015, Oklahoma's recent earthquakes and saltwater disposal: Science Advances, **1**, e1500195, doi: 10.1126/sciadv.1500195.
Walsh, F. R., III, and M. D. Zoback, 2016, Probabilistic assessment of potential fault slip related to injection-induced earthquakes: Application to north-central Oklahoma, USA: Geology, **44**, 991–994, doi: 10.1130/G38275.1.
Walter, J. I., P. Ogwari, A. Thiel, F. Ferrer, I. Woelfel, J. C. Chang, A. P. Darold, and A. A. Holland, 2020, The Oklahoma geological survey statewide seismic network: Seismological Research Letters, **91**, 611–621, doi: 10.1785/0220190211.
Weingarten, M., S. Ge, J. W. Godt, B. A. Bekins, and J. L. Rubinstein, 2015, High-rate injection is associated with the increase in US mid-continent seismicity: Science, **348**, 1336–1340, doi: 10.1126/science.aab1345.

Swetal Patel received a B-Tech (2011) in petroleum engineering in India, an M.S. (2015) in petroleum engineering, and a Ph.D. (2020) in geophysics from the University of Oklahoma. He has worked as a research assistant at the Integrated Core Characterization Laboratory for three years, conducting experiments on hydraulic fracturing and acoustic emissions to understand fatigue's effect on fracture growth and propagation. He further conducted research in the Attribute-Assisted Seismic Processing & Interpretation laboratory in integrating rock physics, geology, and geophysics to map production heterogeneity in unconventional resource plays and mapping reservoir changes caused by hydraulic fracturing using 4D seismic calibration and interpretation. His research interests include amplitude variation with offset, 4D seis-

mic, seismic data conditioning, reservoir characterization by integrating rock physics, and machine learning.

Folarin Kolawole received a B.S. (2008) in geology from Nigeria, an M.S. (2017) in geology from Oklahoma State University, U.S., and a Ph.D. (2020) in geophysics from the University of Oklahoma, U.S. He currently works as a structural geologist with BP America, exploring the rifted margins in South America. His research interests include the structural inheritance and fault reactivation mechanics of injection-induced seismicity and geothermal systems and strain localization in the early stages of continental rifting.

Kurt J. Marfurt received a Ph.D. (1978) in applied geophysics from Columbia University's Henry Krumb School of Mines in New York, where he also taught as an assistant professor for four years. He joined the University of Oklahoma (OU) in 2007, where he serves as the Frank and Henrietta Schultz professor of geophysics within the ConocoPhillips School of Geology and Geophysics. He worked for 18 years in a wide range of research projects at Amoco's Tulsa Research Center, after which he joined the University of Houston for eight years as a professor of geophysics and the director of the Allied Geophysics Lab. He has received the following recognitions: SEG best paper (for coherence), SEG best presentation (for seismic modeling), as a coauthor with Satinder Chopra for best SEG poster (for curvature) and best AAPG technical presentation, and as a coauthor with Roderick Perez-Altamar for best paper in *Interpretation* (on a resource play case study). He also served as the SEG/EAGE Distinguished Short Course Instructor for 2006 (on seismic attributes). In addition to teaching and research duties at OU, he leads short courses on attributes for SEG and AAPG. He currently serves as deputy editor of the SEG/AAPG publication *Interpretation*. His primary research interests include the development and calibration of new seismic attributes to aid in seismic processing, seismic interpretation, and reservoir characterization. Recent work has focused on applying coherence, spectral decomposition, structure-oriented filtering, and volumetric curvature to mapping fractures and karst with a particular focus on resource plays.

Biographies and photographs of the other authors are not available.